PAPER

ECT Attention Reverse Mapping algorithm: visualization of flow pattern heatmap based on convolutional neural network and its impact on ECT image reconstruction

View the article online for updates and enhancements.

ECT Attention Reverse Mapping algorithm: visualization of flow pattern heatmap based on convolutional neural network and its impact on ECT image reconstruction

Zhuoqun Xu[1], **Fan Wu**[2], **Yiyuan Yang**[1] **and Yi Li**[1]

[1] Graduate School at Shenzhen, Tsinghua University, Shenzhen 518055, People's Republic of China
[2] University of Science and Technology of China, Suzhou 215000, People's Republic of China

CrossMark

Abstract
The flow pattern is one of the most basic characteristic parameters of oil–gas two-phase flow, and it has a great influence on the accurate measurement of other parameters of two-phase flow. Over the past decade, the convolutional neural network (CNN) algorithm has been widely used in flow pattern research. Unfortunately, the flow pattern research based on the CNN algorithm is more on model structure optimization, and there is still little insight into the relationship between the CNN algorithm and the physical meaning of the flow pattern. Thus, in this paper, inspired by the neural network visualization gradient-based class activation mapping (Grad-CAM) method, we propose the electrical capacitance tomography (ECT) Attention Reverse Mapping algorithm (EARM) to explore the relationship between the physical meaning of flow patterns and the CNN algorithm. Specifically, the Grad-CAM method is used to obtain heatmaps of flow patterns, and the EARM algorithm combines the hotspot information of the flow pattern heatmap with the ECT image reconstruction principle, which deeply explores the relationship between the CNN flow pattern identification and the ECT image reconstruction algorithm. Furthermore, we conduct prediction experiments based on the parameters of the flow pattern hotspot capacitance data, and the experimental results are compared with the ECT original capacitance data parameter prediction. The prediction accuracy of oil–gas two-phase flow parameters has been improved by more than 50% on average, and experiments have verified the correctness of the visualization of CNN network flow pattern identification.

Keywords: neural network interpretability, gradient-based class activation mapping model, flow pattern heatmap, convolutional neural network, ECT image reconstruction, flow rate prediction, electrical capacitance tomography

(Some figures may appear in colour only in the online journal)

1. Introduction

Oil–gas two-phase flow exists widely in the petroleum industry. In recent years, various parameters of oil–gas two-phase flow have been widely studied. The correct measurement of oil–gas two-phase flow parameters has great significance for the rational and safe exploitation of oil [1]. The flow pattern is an important parameter of oil–gas two-phase flow. It not only affects the flow morphology, heat, and mass transfer performance of two-phase flow, but also has a profound an impact on the accurate measurement of other parameters of oil–gas two-phase flow [2]. Currently, many
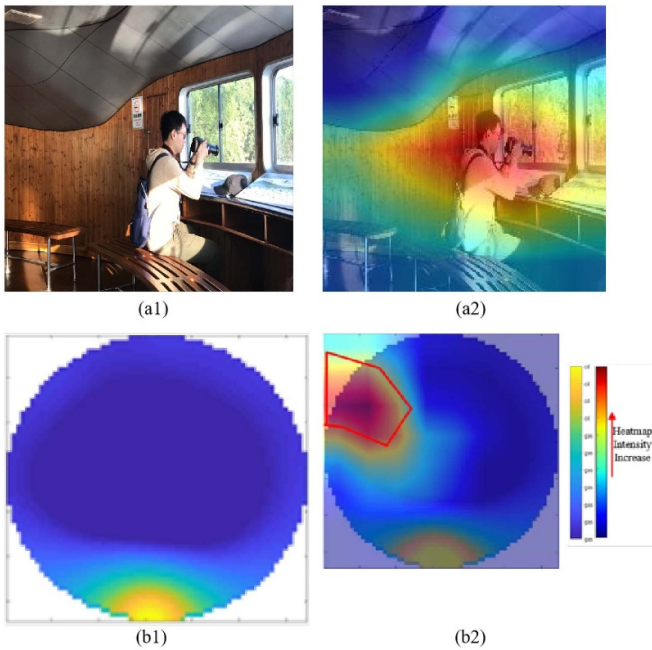
Figure 1. The recognition result of the picture heatmap. (a1) The original picture of the person. (a2) The heatmap of the person. (b1) The original picture of the ECT image. (b2) The heatmap of the ECT image.

articles use neural network methods to classify and identify flow patterns, but only extract the surface information of flow patterns for research and analysis, and do not deeply explore information about flow patterns. In this paper, the heatmap of the flow pattern is studied for the first time, and the connection between the flow rate parameters and the reconstructed image is explored, such as the internal mechanism of hotspot distribution in a flow pattern heatmap (as shown in figure 1).

Figure 1 shows the recognition results of the heatmap of the picture. (a1) and (a2) shows the recognition results of the heatmap of the person picture, where the hotspot area represents the main recognition area recognized by the convolutional neural network (CNN) network. (b1) and (b2) show the heatmap recognition results of the flow pattern. The area marked with a red circle in figure 1 (b2) is the hotspot area for CNN network flow pattern recognition; that is, the main recognition flow pattern area. It can be seen from figure 1 that under this flow pattern condition, the main recognition area of the CNN network flow pattern recognition is the upper left area of the flow pattern.

At present, the main hardware devices used to obtain the oil–gas two-phase flow pattern include high-speed cameras [3], wire-mesh sensors [4], microwave sensors [5], ultrasonic sensors [6], and electrical sensors. Da Silva *et al* used a wire-mesh sensor to measure the oil–gas two-phase flow pattern, and the sensor had a measurement speed of 5000 frames per second [7]. López *et al* used a high-speed camera to measure the flow pattern of oil–gas two-phase flow, and converted the flow pattern diagram to a black and white image for analysis by threshold technology [8]. Rahiman *et al* used an ultrasonic

doppler sensor to measure the flow velocity of oil–gas two-phase flow and reconstruct the flow pattern. When the image reconstruction speed was 10 frames per second, its performance was optimal [9]. Although the above sensors can realize flow pattern recognition, they all have their own defects. Among them, high-speed camera equipment is expensive and requires a high measurement environment, which is not suitable for field environment measurement of the oil field. The wire-mesh sensor has a complex structure, making field maintenance difficult in oil fields. The ultrasonic sensor has a low measurement accuracy and cannot meet the high-accuracy requirements of the experiment. Therefore, electrical sensors are designed and applied for parameter measurement and flow pattern identification of multiphase flow. Meng *et al* used an electrical resistance tomography (ERT) sensor to identify the gas–water two-phase flow pattern, and used the least squares support vector machine method to establish the gas flow rate measurement model for gas–water two-phase flow [10]. Li *et al* used the capacitance value obtained by the electrical capacitance tomography (ECT) sensor to perform real-time identification of oil–gas two-phase flow patterns and measure the gas flow rate based on the results of the flow pattern prediction [11]. Compared with other sensors, electrical sensors have the advantages of low cost, high equipment accuracy, and mature product development. They are widely used in flow pattern recognition of oil–gas two-phase flows.

For flow pattern identification of oil–gas two-phase flow, the commonly used methods are the visual observation method [12], conductivity probe detection method [13], particle image velocimetry (PIV) [14], and dual-impedance probe measurement method [15]. Charles and Lilleleht used a combination of camera shooting and visual observation to measure gas–liquid two-phase flow patterns [16]. Augier *et al* used PIV to measure oil–water two-phase flow patterns [17], and Lovick and Angeli used a dual-impedance probe to measure the droplet distribution in oil–water two-phase flow [15]. Hanafizadeh *et al* proposed a method for identifying the vertical pipe flow pattern. Fifteen pressure transmitters were placed at different positions in the vertical pipe, and the gas–water two-phase flow pattern was predicted based on the average pressure and pressure fluctuation data [18]. Compared with the traditional method of flow pattern identification, the neural network has low cost and demonstrates a significant increase in identification accuracy and greatly improved identification efficiency. To date, many studies have identified and predicted flow patterns based on neural network models. Roshani *et al* used the artificial neural network algorithm combined with the gamma-ray attenuation method to identify the flow pattern of gas–liquid two-phase flow and predict the voidage [19]. Hu *et al* introduced the method of speech emotion feature identification to flow pattern identification, and input the extracted electrostatic wave signal into the backpropagation (neural network for flow pattern identification. The flow pattern identification rate reached 97% [20]. Zhou *et al* used the independent component analysis radial basis function model to extract characteristic parameters of the flow pattern and identify the flow pattern for the gas–liquid two-phase flow [21]. However, current oil–gas two-phase flow identification methods only use neural network

models for flow pattern identification and flow rate prediction, and do not explore the relationship between neural networks and the physical meanings associated with image reconstruction algorithms. They lack the interpretability of neural network flow pattern identification. In this paper, by studying the heatmap of the oil–gas two-phase flow pattern, the internal principle of the neural network identification flow pattern is analyzed, and the relationship between the neural network and the physical meaning of the image reconstruction algorithm is explored.

In various fields such as image classification, object detection, and semantic segmentation, CNNs and other deep neural networks have highlighted their superior performance [22]. Improving the interpretability of neural networks has been a wide concern and has become a current research hotspot. The visualization method is the most widely used method in data-based interpretability analysis. The visualization method mainly labels important parts of the data through visualization tools, and combines the neural network learning process with the original measurement data, so that we can understand the learning process of deep learning more clearly [23]. Selvaraju *et al* used a visualization method to generate a heatmap of the gradient of the convolutional layer in the CNN network, thereby displaying and labeling the important pixels of the input image, which improved our understanding of the learning area of deep learning [24]. The visualization method of the heatmap provides a more direct understanding of the internal mechanism of neural networks. In the study of oil–gas two-phase flow parameters, neural networks are widely used. Yang *et al* used the U-net model in a CNN network for flow pattern identification [25], and Xu *et al* used the CNN model to predict the parameters of oil–gas two-phase flows based on the flow pattern [26]. At present, neural networks are only in the application stage in the field of two-phase flow parameter measurement. The relationship between neural networks and the true physical meaning of two-phase flow parameters has not been explored. It lacks the interpretability of neural networks. Therefore, for the first time, this paper studies the heatmap of the oil–gas two-phase flow pattern. By analyzing the heatmap of the flow pattern, the relationship between the neural network and the physical meaning of the image reconstruction algorithm is explored. This paper proposes the ECT Attention Reverse Mapping algorithm (EARM), which includes a neural network heatmap to mine the true physical meaning of each position of the flow pattern obtained by image reconstruction.

The research in this paper is of great significance to the development of petroleum and other related companies. It reduces industrial production operating costs and improves industrial production efficiency through advanced technical means. The main contributions of this paper are as follows.

(a) We propose the EARM algorithm, which realizes the visualization of CNN network flow pattern identification. By studying the heatmap of the oil–gas two-phase flow pattern, the true physical meaning of each position of the flow pattern is deeply explored, and the relationship between

the neural network and the physical meaning of the image reconstruction algorithm is explored.

(b) We conduct a parameter prediction experiment based on flow pattern hotspot capacitance data, and prove the correctness of the proposed CNN network flow pattern identification visualization. This improves the robustness and adaptability of the CNN algorithm in the field of flow pattern research, and has positive significance for the subsequent optimization of the CNN network in ECT image reconstruction.

In the rest of this paper, section 2 describes the methodology of flow pattern analysis and visualization methods. Section 3 draws and analyzes flow pattern heatmaps under different working conditions. Section 4 describes the ECT Attention Reverse Mapping algorithm. Section 5 shows and analyzes the experimental results of the EARM algorithm. Section 6 gives a full-text summary and future research directions.

2. Methodology

2.1. Application of CNN in multiphase flow

In recent years, artificial intelligence technology has developed rapidly, and deep learning has been applied to more and more fields. CNNs, as one of the representative algorithms for deep learning, are mainly used for image identification. In the current research of multiphase flow, especially in the fields of image reconstruction, flow pattern identification, and yield prediction, CNN technology is widely used.

Tan *et al* [27] used a CNN for ERT image reconstruction. The CNN algorithm has good generalization for image reconstruction. Compared with the flow pattern obtained by the traditional image reconstruction algorithm, that obtained by the CNN algorithm is more accurate; that is, it is closer to the real distribution of the flow pattern in the pipeline. Dang *et al* [28] optimized the sensor hardware model and established a measurement model based on CNN-LSTM to measure the flow parameters of multiphase flows with high accuracy. Du *et al* [29] used a CNN to identify oil–water two-phase flow patterns, and used the LeNet-5, AlexNet, and VGG-16 models to identify flow patterns. Experimental results show that deeper network structures have higher accuracy. In the current research, the CNN network only stays at the application stage in the field of multiphase flow. The CNN network is often used for flow pattern identification and parameter measurement of multiphase flow. At present, no research has explored the relationship between CNNs and the physical meaning of multiphase flow measurement models. In the field of multiphase flow, exploring the inherent mechanism of CNN identification and prediction can help improve the accuracy of prediction.

CNNs are mainly used for image identification, so in the field of multiphase flow measurement, the most applied directions for CNN models are image reconstruction and flow pattern prediction. The current commonly used ECT image reconstruction algorithms include the linear projection algorithm, Tikhonov regularization algorithm, Landweber algorithm, etc.

There has been much research on the improvement of the ECT image reconstruction algorithm. Yang and Peng analyzed the influence of the capacitance between different electrode pairs in ECT sensors on the flow patterns at different positions. The experimental results show that the adjacent electrode pairs are most sensitive to the change of the dielectric constant at the container wall, and have little effect on the flow pattern's center area. The opposite electrode is more sensitive to changes in the central area, and the spacer electrode is more sensitive to changes in the sub-central area [30]. This study explores the distribution of capacitance values from the perspective of image reconstruction, but currently there is no research exploring the relationship between image reconstruction algorithms and CNNs. Inspired by the above, based on the gradient-based class activation mapping (Grad-CAM) method and ECT image reconstruction algorithm, this paper proposes an EARM algorithm for mining the internal mechanism and connection between the CNN network and the image reconstruction algorithm.

2.2. Relevant background for heatmap research

For a long time, although the CNN algorithm has obvious effects, it has been controversial because of its poor interpretability. Selvaraju *et al* proposed a method of CNN network interpretability, displaying the features learned by the CNN network in the form of a heatmap, in order to find the focus of the CNN model; that is, the hotspot. Grad-CAM is a commonly used visualization model for obtaining heatmaps of images. The steps of Grad-CAM to solve the heatmap are as follows. First, it finds the feature map obtained by image extraction after feature extraction and the last convolution. Each feature map has different weights in the fully connected layer, and the weight of each feature map is obtained by back-propagation. The weight solution formula of Grad-CAM is shown in formula (1).

$$\beta_q^a = \frac{1}{K} \sum_m \sum_n \frac{\partial x^a}{\partial B_{mn}^q} \tag{1}$$

In formula (1), β_q^α represents the weight of the qth feature map corresponding to the class α, k is the expected number of feature maps, x^α is the gradient of the score for class α, and B_{mn}^q is the expected value of the (m, n) position in the qth feature map. Each feature map is multiplied by the weight to obtain a weighted feature map, and all feature maps are summed and activated using the Relu function. The calculation formula is shown in formula (2).

$$L_{Grad-CAM}^a = Relu \left(\sum_q \beta_q^a B^q \right) \tag{2}$$

In formula (2), only the features useful for the category are retained after the Relu activation function, where positive numbers represent features useful for the category, and negative numbers represent features useful for other categories (i.e. useless features). If there is no Relu activation function, the heatmap represents multi-category features. Finally,
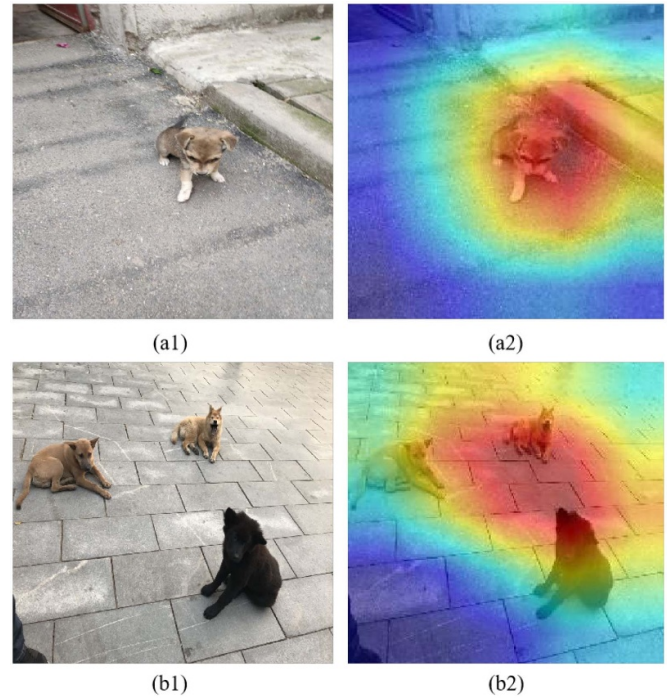
Figure 2. Effect of heatmap identification. (a1) Single-target identification original image. (a2) Single-target identification heatmap. (b1) Multi-target identification original image. (b2) Multi-target identification heatmap.
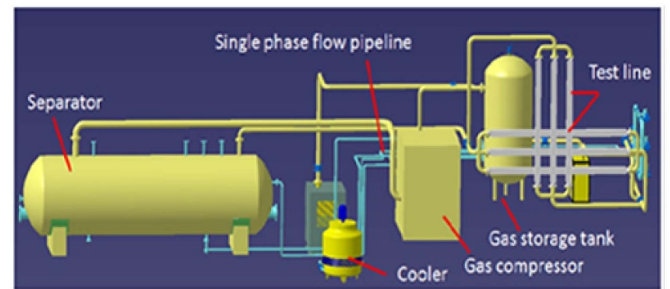
Figure 3. Schematic diagram of experimental equipment.

the heatmap is scaled to the image size to facilitate weighting with the image. Figure 2 shows the original image and heatmap of the single target and multiple targets identified using the CNN + Grad-CAM model.

3. Flow pattern heatmap analysis

The experimental data are collected through the semi-industrial multiphase flow experimental measurement platform. A schematic diagram of the platform is shown in figure 3.

Figure 3 shows the experimental platform of this experiment, in which oil is stored in the separator, gas is generated by the gas-phase compressor, and the oil phase and the gas phase are mixed and pass through the test pipeline. The experimental equipment is distributed in sequence on the pipeline, followed by an upstream ECT sensor, venturi tube,

Table 1. Working condition distribution table (m³ h⁻¹).

Gas													
Oil	1	1.5	2	2.5	3	3.5	4	4.5	5	6	7	8	10
20	Case₁	Case₅	Case₉	Case₁₃	Case₁₇	Case₂₁	Case₂₅	Case₂₉	Case₃₃	Case₃₇	Case₄₁	Case₄₅	Case₄₉
50	Case₂	Case₆	Case₁₀	Case₁₄	Case₁₈	Case₂₂	Case₂₆	Case₃₀	Case₃₄	Case₃₈	Case₄₂	Case₄₆	Case₅₀
90	Case₃	Case₇	Case₁₁	Case₁₅	Case₁₉	Case₂₃	Case₂₇	Case₃₁	Case₃₅	Case₃₉	Case₄₃	Case₄₇	Case₅₁
150	Case₄	Case₈	Case₁₂	Case₁₆	Case₂₀	Case₂₄	Case₂₈	Case₃₂	Case₃₆	Case₄₀	Case₄₄	Case₄₈	Case₅₂
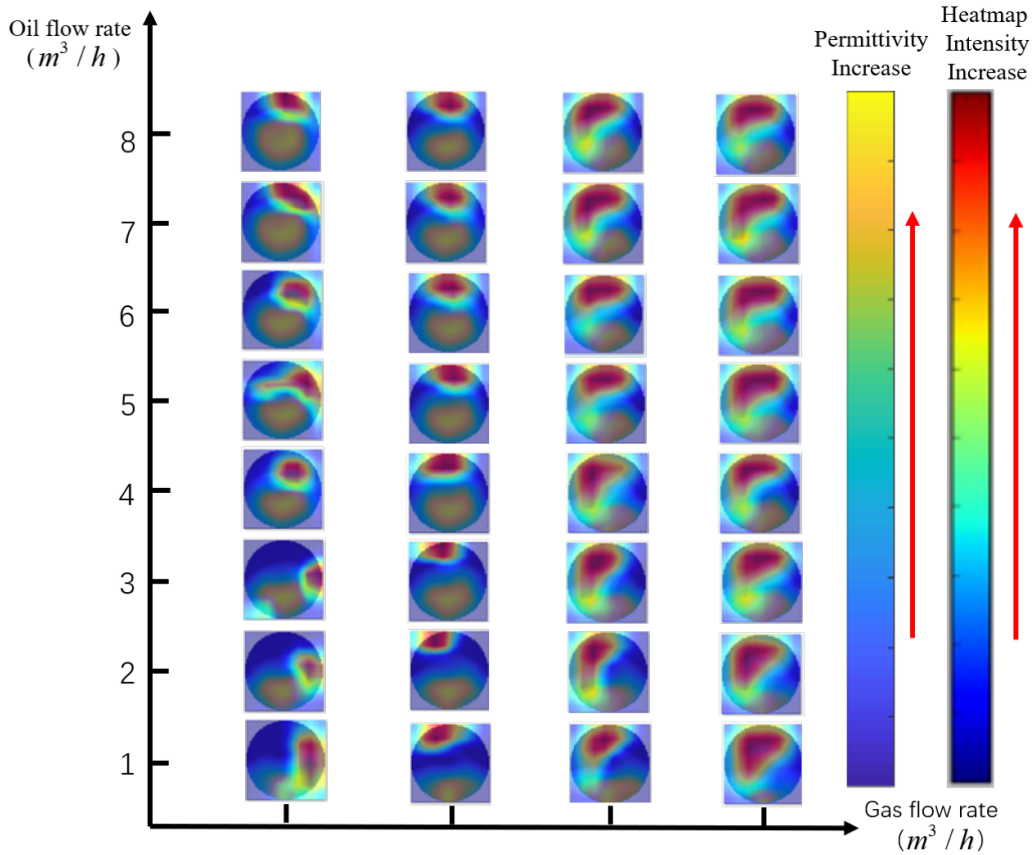
Figure 4. Heatmap of the ECT image upstream of the venturi tube.

and downstream ECT sensor. The specific parameters of the ECT sensor and venturi tube are provided in the literature [31]. The oil–gas two-phase flow passes through the pipeline equipment for parameter measurement in sequence, and different working conditions are set during the experiment; the oil flow rate and gas flow rate under each working condition are different. Table 1 shows the oil flow rate and gas flow rate under different working conditions.

As shown in table 1, a total of 52 working conditions have been designed, in which the distribution range of the oil flow rate is 1–10 m³ h⁻¹, and the distribution range of the gas flow rate is 20–150 m³ h⁻¹. The specific experimental equipment parameters and experimental methods are described in the literature [31].

The capacitance values measured by the ECT sensor under different working conditions are obtained through experiments. The linear back-projection algorithm is used to get the grayscale permittivity distribution image, and then get the flow pattern of the oil–gas two-phase flow. In this paper, we obtain

the flow pattern of the oil–gas two-phase flow upstream and downstream of the venturi tube.

Based on the Inception-V3 model in the CNN network, the Grad-CAM method is used to realize the visualization of the neural network identification flow pattern. The Relu activation function is used in the Inception-V3 model, and its expression is shown in formula (3).

$$f(x) = \max(x, 0) \tag{3}$$

The loss function of this model uses the mean-square error (MSE) loss function, and its expression is shown in formula (4).

$$\text{Loss} = \frac{\sum_{i=1}^{n} (y_i - y_i^p)^2}{n} \tag{4}$$

In formula (4), y_i represents the true oil flow rate and gas flow rate, y_i^p represents the predicted oil flow rate and gas flow rate, and n is 2.

The Grad-CAM algorithm is used to generate the heatmap of the convolution layer's gradient of the Inception-V3 model. The capacitance data of the ECT sensor under 52 working conditions are measured through experiments, and the flow patterns under different working conditions are obtained through the linear back-projection (LBP) image reconstruction algorithm. Through the Grad-CAM algorithm, heatmaps of the flow patterns under different working conditions are generated. In the experiment, the flow patterns of oil–gas two-phase flow upstream and downstream of the venturi tube are measured separately, so this paper respectively analyzes the heatmaps of the flow patterns upstream and downstream of the venturi tube. Figure 4 shows the heatmap of the flow pattern upstream of the venturi tube.

Figure 4 shows the distribution of hotspots in the flow pattern heatmap upstream of the venturi tube. Under different gas flow rate conditions, the distribution of hotspots in the heatmap is different. When the gas flow rate is small (gas flow rate is 20 m^3 h^{-1}), the hotspots of the heatmap are mainly distributed on the right side of the flow pattern. When the gas flow rate is large (gas flow rate is 50 m^3 h^{-1}), the hotspots of the heatmap are mainly distributed on the upper side of the flow pattern. When the gas flow rate continues to increase (the gas flow rate is 90–140 m^3 h^{-1}), the hotspots of the heatmap are mainly distributed on the upper left side of the flow pattern. With the increase of the gas flow rate, the distribution of hotspots in the flow pattern heatmap shows a counterclockwise rotation trend. The analysis of the distribution of hotspots in the flow pattern heatmap shows that the CNN network has different concerns in identifying the flow pattern at different flow rates. Figure 5 shows the analysis of the heatmap of the flow pattern downstream of the venturi tube.

Figure 5 shows the heatmap of the flow pattern downstream of the venturi tube. When the gas flow rate is small (gas flow rate is 20 m^3 h^{-1}), the hotspots of the heatmap are mainly distributed on the left side of the flow pattern. As the gas flow rate increases (gas flow rate is 50–140), the hotspots of the heatmap are mainly distributed on the upper left side of the flow pattern. When the gas flow rate is 50 m^3 h^{-1}, the hotspot area of the heatmap is distributed in the top left corner of the image. A possible reason is that the flow pattern is mainly slug flow and annular flow under this gas flow rate. However, the oil phase distribution of the ECT image of the oil–gas two-phase flow is not concentrated in the top left corner of the pipeline. In the case that the annular flow or the slug flow is close to the annular flow, the oil phase will reach the top left corner of the ECT image. The top left corner area of the ECT image can better reflect the change characteristics of the flow pattern. The neural network mainly identifies the flow pattern with changing characteristics. Therefore, when the gas flow rate in figure 5 is 50 m^3 h^{-1}, the neural network mainly identifies the area in the top left corner of the ECT image. Compared with the heatmap upstream of the venturi tube, the hotspot distribution on the heatmap downstream of the venturi tube is more stable. In this paper, according to the different characteristics of the hotspot distribution of the flow pattern heatmap, combined with the physical principle of ECT image reconstruction, an EARM algorithm is proposed to mine the internal mechanism and connection between the neural network and the image reconstruction algorithm.

4. EARM algorithm

Algorithm 1: EARM

Input: $\{cap|cap \in Work\_Condition[i], 0 \leq i \leq 52\}$
Output: Cap_Best\{\}
1 Cap_New\{\} $\longleftarrow \emptyset$;
2 Cap_Contrast1\{\} $\longleftarrow \emptyset$;
3 Cap_Contrast2\{\} $\longleftarrow \emptyset$;
4 Cap_Best\{\} $\longleftarrow \emptyset$;
5 **foreach**
  $work\_con \longleftarrow Work\_Condition[i], i \in (0,52)$ **do**
6   **foreach** $cap \in work\_con$ **do**
7      $Ect\_img \longleftarrow$ LBP(cap);
8      $Heatmap \longleftarrow$ Grad_cam(Ect_img);
9   Through $Heatmap$ get $hotspot$;
10     $cap\_new \longleftarrow$ Update
      ($hotspot, cap, Del\_threshold$);
11     $cap\_contrast1 \longleftarrow$ Update
      ($hotspot, cap, Del\_threshold\_small$);
12     $cap\_contrast2 \longleftarrow$ Update
      ($hotspot, cap, Del\_threshold\_large$);
13   Insert cap_new, $cap\_contrast1$ and $cap\_contrast2$
      respectively in Cap_New{}, Cap_Contrast1{} and
      Cap_Contrast2{};
14   **end**
15   **for** $cap\_temp[1]$, $cap\_temp[2]$ and $cap\_temp[3]$
     $\in Cap\_New\{\}$, $Cap\_Contrast1\{\}$ and
     $Cap\_Contrast2\{\}$ **do**
16     $acc1, acc2, acc3 \longleftarrow$ CNN(cap_temp1,
      cap_temp2 , cap_temp3);
17     $acc\_best\_coordinate \longleftarrow$ Max($acc1, acc2, acc3$);
18   Get the $cap\_temp[n]$ corresponding to
      $acc\_best\_coordinate$;
19   Cap_Best.append($cap\_temp[n]$);
20   **end**
21   **return** Cap_Best
22 **end**

According to figures 4 and 5, under different gas flow rate conditions, the distribution of hotspots in the ECT sensor flow pattern heatmap obtained by the CNN and= Grad-CAM model is different. This shows that under different flow rate conditions, the CNN network has different attention positions for flow pattern identification. That is to say, when the CNN network performs flow pattern identification, it does not use equal weights to identify each part of the entire flow pattern. The CNN network has different identification weights for each area of the flow pattern, and the position of large weights (i.e. hotspots) has the greatest effect on flow pattern identification. Therefore, this paper proposes the EARM, which extracts effective information on the flow pattern of the hotspot area of the flow pattern heatmap, combines the identification mechanism of the CNN model
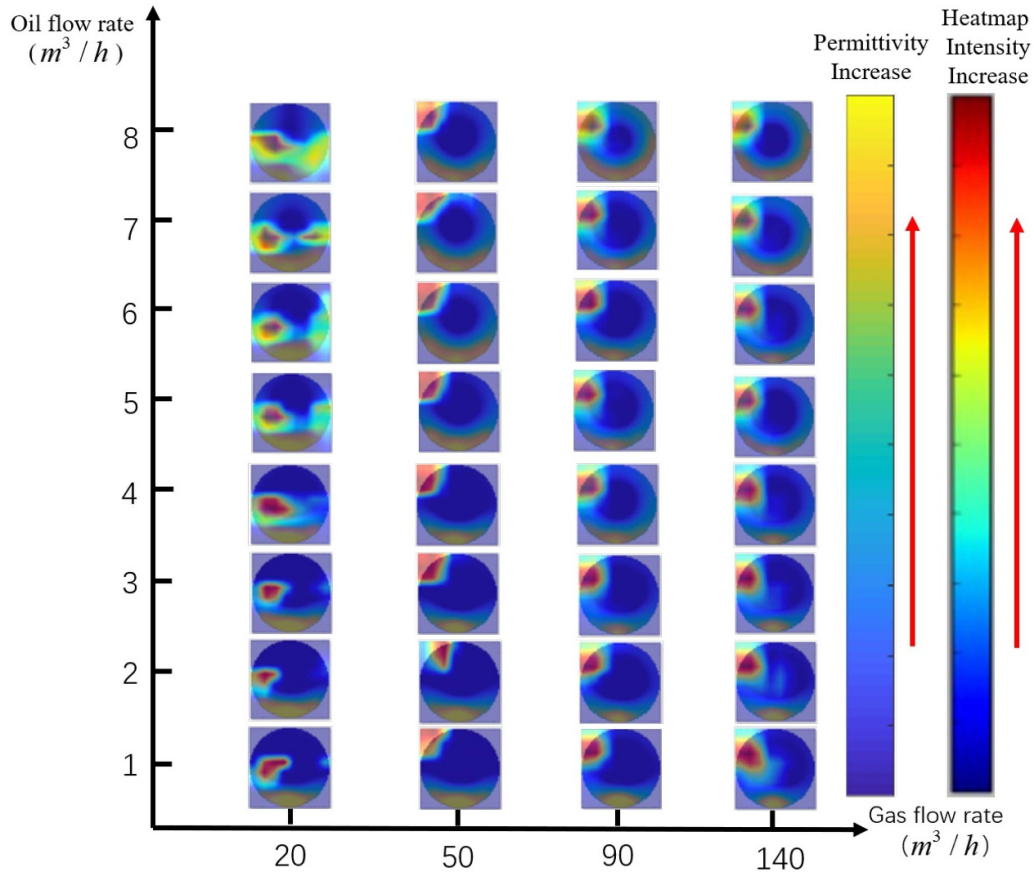
Figure 5. Heatmap of the ECT image downstream of the venturi tube.

with the physical principle of ECT sensor image reconstruction, improves the ECT measurement model, and effectively improves the flow pattern identification accuracy of the CNN network. Algorithm 1 shows the flowchart of the EARM algorithm.

As shown in Algorithm 1, our main process is as follows:

- *cap* represents a group of capacitance values collected through experiments, and *work_con* represents the working condition corresponding to the capacitances. First determine that the *work_con* corresponding to this set of capacitances meets the *Work_Condition* distribution in table 1.
- *ECT_img* represents the flow pattern obtained through the *LBP* image reconstruction algorithm. Use the *LBP* algorithm to reconstruct the *cap* to get the *ECT_img*, use the *Grad_cam* model to get the *Heatmap* of *ECT_img*, and get the *hotspot* through the *Heatmap*.
- Based on the sensitivity distribution of the ECT sensor, the effective capacitance of the *cap* is extracted through *hotspot* to obtain *cap_new*.
- Based on the expansion and deletion of *hotspot* areas, two sets of contrast experiments were designed to obtain *cap_contrast1* and *cap_contrast2*.
- Use the CNN model to compare the prediction accuracy of the three sets of capacitances of *cap_new*, *cap_contrast1* and *cap_contrast2*, and select the set of capacitances with the highest prediction accuracy as *Cap_Best*.

The effective capacitance of the ECT sensor can be obtained through the EARM algorithm. Using the effective capacitance to predict the oil–gas two-phase flow parameters can improve the flow rate prediction accuracy.

Eight electrode plates are evenly distributed inside the tube wall of the ECT sensor, and any two pairs of electrode plates form an electrode pair. When one of the electrodes is excited and the other electrode is maintained at zero potential, a capacitance is formed and capacitance data are generated. The number of independent capacitors measured by the ECT sensor is: $N(N-1)/2$. Therefore, the eight-electrode ECT sensor generates 28 sets of independent capacitance data. Based on the capacitance data measured by the ECT sensor, the image reconstruction algorithm is used to obtain the flow pattern. The change in capacitance between each pair of electrode plates has the greatest influence on the flow pattern of the connection area of the two electrode plates [30]. Figure 6 shows the sensitivity distribution of electrode plates with different intervals.

Figure 6 shows the typical sensitivity distribution of the ECT sensor, and the value on the right side of the color chart shows the sensitivity value. It can be seen from figure 6 that the electrode plate combinations with different intervals have different influence areas on the flow pattern. The combination of adjacent electrode plates has the greatest impact on the area near the wall of the tube, and basically has no effect on the central area. The sub-adjacent electrode plate combination
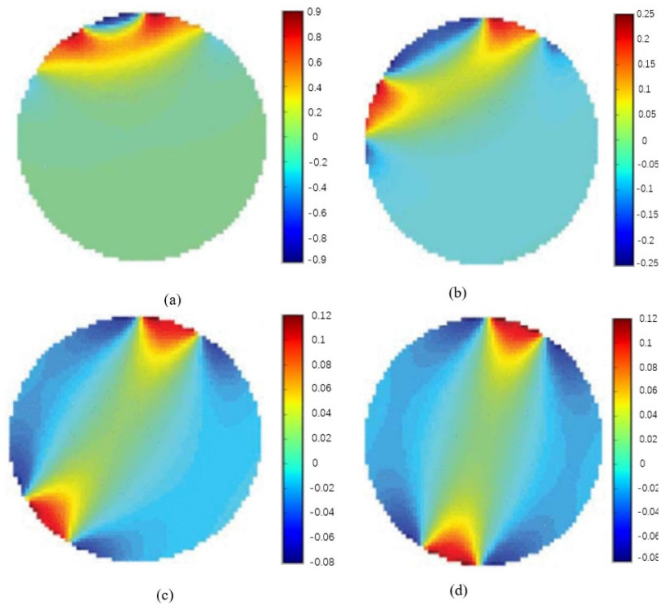
Figure 6. Sensitivity distribution of eight-electrode ECT sensor. (a) Sensitivity distribution of adjacent electrode pairs. (b) Sensitivity distribution of single-spaced electrode pairs. (c) Sensitivity distribution of double-spaced electrode pairs. (d) Sensitivity distribution of opposite electrode pairs.
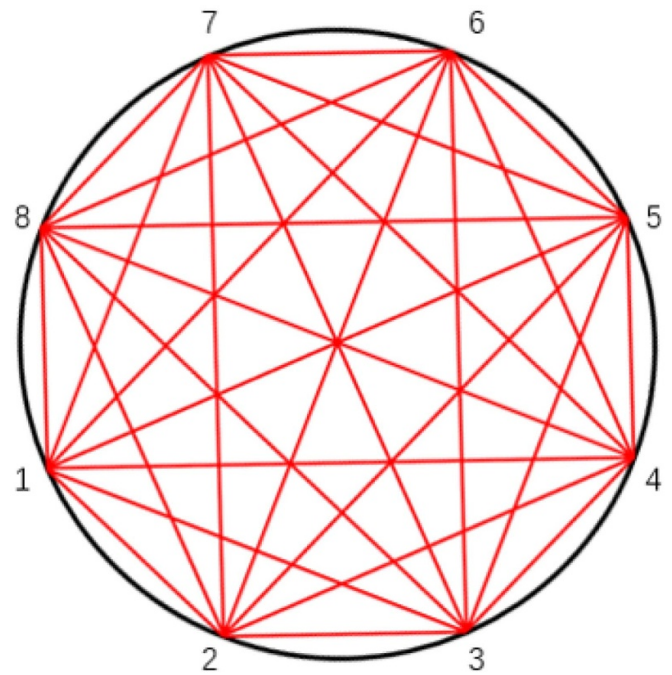

Figure 7. Schematic diagram of capacitance distribution of ECT sensor cross-section.

has the greatest influence on the sub-center area. The opposite electrode plate combination has the greatest influence on the central area and the least influence on the tube wall area. Overall, the combination of electrode plates with different intervals contributes the most to the flow pattern in the connecting area of the two electrode plates, and has less impact on other areas [30]. Therefore, based on this phenomenon, combined with the hotspot area distribution of the flow pattern heatmap calculated above, we extract the independent capacitance data of the hotspot area, and compare the capacitance value extracted based on the heatmap hotspot with the original capacitance value of the ECT sensor. The important influence of CNN network flow pattern identification visualization on ECT image reconstruction and oil–gas two-phase flow measurement is highlighted. Figure 7 shows the capacitance distribution of the ECT sensor cross-section.

In figure 7, the eight vertices represent the eight electrode plates inside the ECT sensor. The area connected between every two electrode plates represents the area with the largest sensitivity distribution of this inter-electrode capacitance in the measuring region. That is, the connection area of every two electrode plates is the area where the electrode contributes most to the flow pattern.

In different areas of the flow pattern, different electrode pairs need to be used for imaging. The eight-electrode ECT sensor produces a total of 28 sets of capacitance values, which are carried out in the order of electrode pairs 1–2, 1–3, 1–4, ..., 2–3, 2–4, ..., 7–8 sort. It can be seen from figure 4 that when the gas flow rate is small (20 m^3 h^{-1}), the hotspots of the heatmap are mainly distributed on the right side of the flow pattern. Figure 8 shows the capacitance distribution of the ECT sensor under the condition of gas flow rate of 20 m^3 h^{-1}.
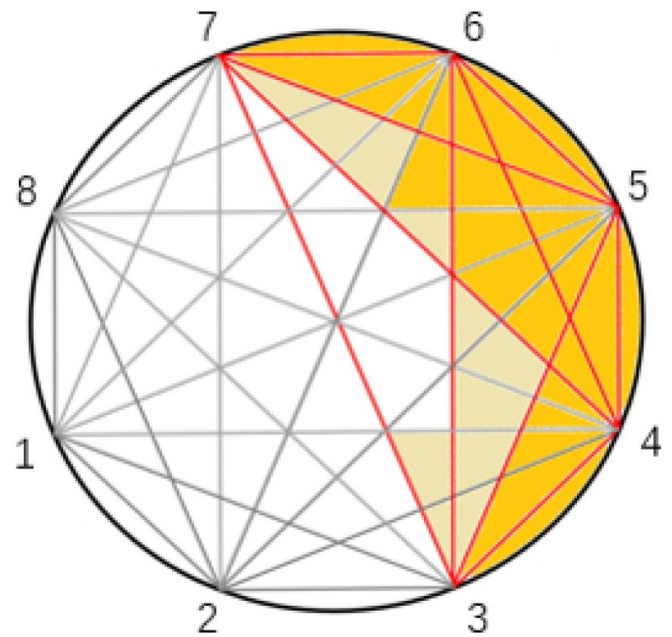
Figure 8. Capacitance distribution of ECT sensor under small gas flow rate.

Figure 8 shows the distribution of effective electrode pairs in the ECT sensor under the condition of gas flow rate of 20 m^3 h^{-1}. The red line indicates the electrode pair that contributes the most to the flow pattern under this gas flow rate. The gray line indicates the electrode pair that does not contribute much to the flow pattern under this gas flow rate. The color in the grid of figure 8 represents the attention degree of CNN network flow pattern identification, and the darker the
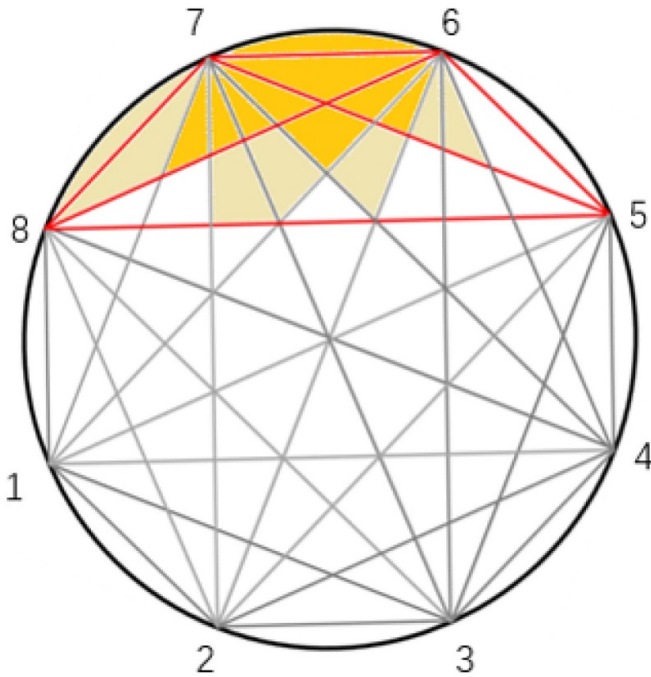
Figure 9. Capacitance distribution of ECT sensor under medium gas flow rate.
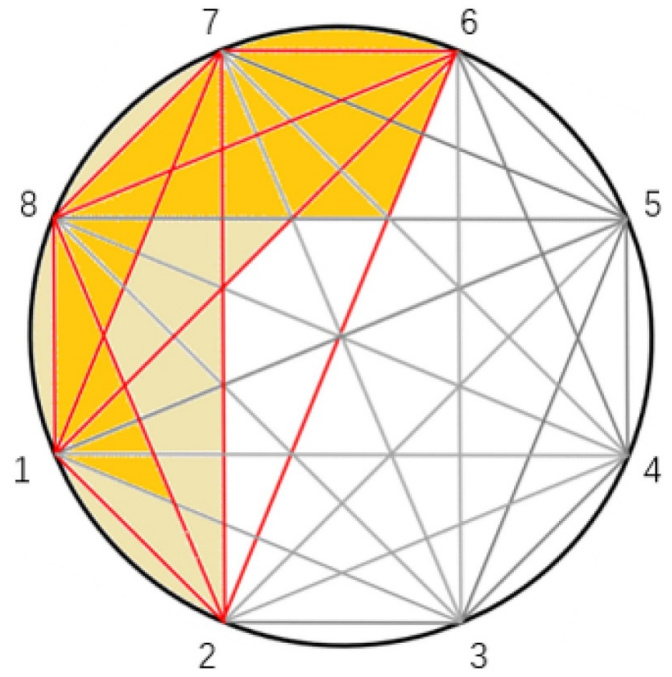
Figure 10. Capacitance distribution of ECT sensor under large gas flow rate.

color in the grid, the higher the importance of the area for CNN network flow pattern identification. Therefore, when using the ECT sensor to measure the oil–gas two-phase flow parameters under this gas flow rate condition, it is not necessary to use all 28 sets of capacitance values generated by the ECT sensor, and only the capacitance values of the hotspot distribution area of the heatmap can be used for measuring the two-phase flow parameters. Under the condition that the gas flow rate is 20 m^3 h^{-1}, the ECT sensor electrode pairs to be used are 3–4, 3–5, 3–6, 3–7, 4–5, 4–6, 4–7, 5–6, 5–6, 5–7, 6–7. By using the 10 extracted sets of capacitance values instead of the original 28 sets of capacitance values, combining the visualization results of CNN network flow pattern identification with the ECT image reconstruction principle, the characteristics used for oil–gas two-phase flow parameter measurement are more significant, and increase parameter prediction accuracy.

Figures 9 and 10, respectively, show the effective electrode pair distribution of the ECT sensor under the conditions of medium gas flow rate and large gas flow rate in the oil–gas two-phase flow.

It can be seen from figure 9 that under the condition of gas flow rate of 50 m^3 h^{-1}, the hotspots of the heatmap are mainly distributed on the upper side of the flow pattern. According to the hotspot distribution of the flow pattern heatmap, under the condition of medium gas flow rate, the electrode pairs of the ECT sensor to be used are 5–6, 5–7, 5–8, 6–7, 6–8, 7–8. Six sets of effective capacitance values are extracted from the hotspot distribution area to replace the 28 sets of original capacitance values of the ECT sensor to measure the oil–gas two-phase flow parameters.

It can be seen from figure 10 that when the gas flow rate is 90 and 150 m^3 h^{-1}, the hotspots of the heatmap are mainly distributed on the upper left side of the flow pattern. According to the hotspot distribution of the flow pattern heatmap, under the condition of large gas flow rate, the electrode pairs of the ECT sensor to be used are 1–2, 1–6, 1–7, 1–8, 2–6, 2–7, 2–8, 6–7, 6–8, 7–8. Therefore, under the conditions of gas flow rate of 90 and 150 m^3 h^{-1}, the oil–gas two-phase flow parameters are predicted by extracting 10 sets of effective capacitance values instead of the original 28 sets of capacitance values.

Figures 8–10, respectively, show the distribution of effective electrode pairs of the flow pattern heatmap upstream of the venturi tube under different gas flow rate conditions. During the collection of experimental data, the capacitance values of the ECT sensors upstream and downstream of the venturi tube are collected to verify the generality of the proposed EARM algorithm. It can be seen from the hotspot distribution of the flow pattern heatmap downstream of the venturi tube shown in figure 5 that the hotspot distribution is mainly divided into two cases. When the gas flow rate is small (20 m^3 h^{-1}), the hotspots of the flow pattern heatmap are mainly distributed on the left side of the flow pattern. As the gas flow rate increases, the hotspots of the flow pattern heatmap are stably distributed on the upper left side of the flow pattern. Figures 11–12, respectively, show the effective capacitance distribution of the ECT sensor downstream of the venturi tube under the conditions of small gas flow rate and large gas flow rate.

As can be seen from figures 11 and 12, for the capacitance data of the ECT sensor downstream of the venturi tube, when the gas flow rate is 20 m^3 h^{-1}, 10 sets of capacitance values 1–2, 1–3, 1–4, 1–8, 2–3, 2–4, 2–8, 3–4, 4–8 are selected instead
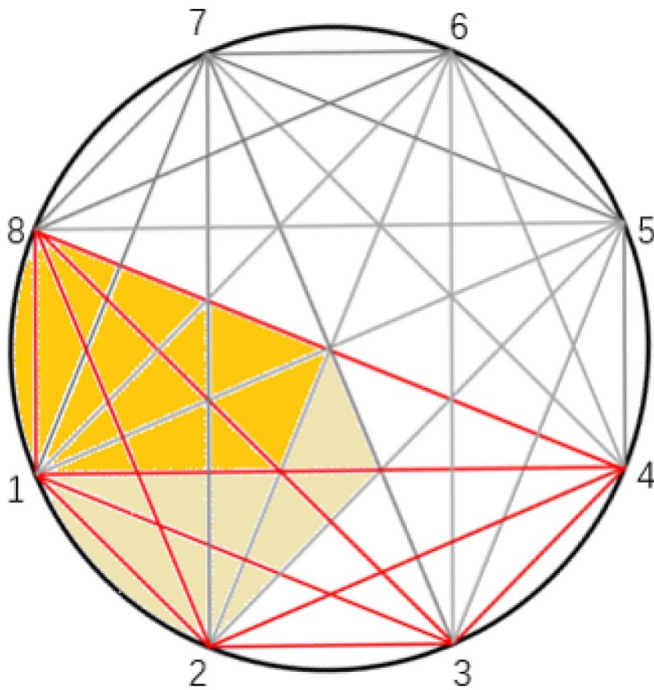
Figure 11. Capacitance distribution of the ECT sensor with small gas flow rate downstream of the venturi tube.
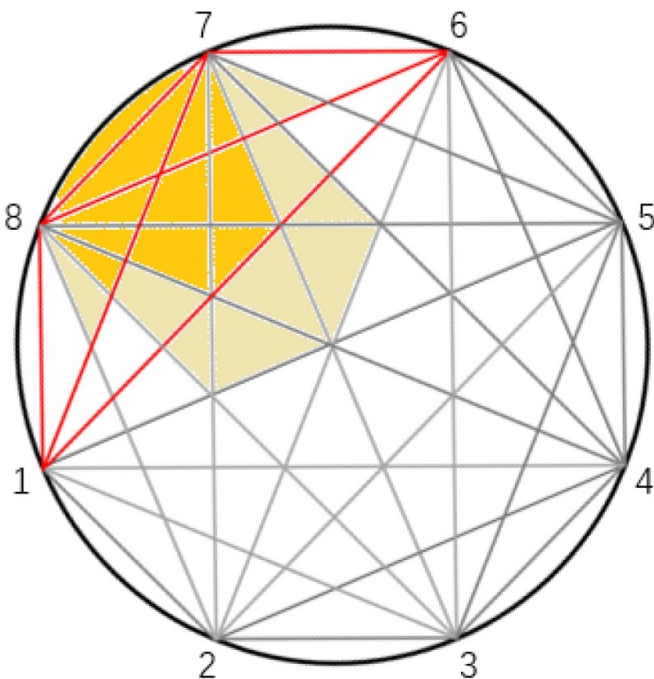
Figure 12. Capacitance distribution of the ECT sensor with large gas flow rate downstream of the venturi tube.

of the original 28 sets of capacitance values generated by the ECT sensor to measure the oil–gas two-phase flow parameters. In the case of gas flow rates of 50, 90, 140 m³ h^{-1}, we select six sets of capacitance values 1–6, 1–7, 1–8, 6–7, 6–8, 7–8 instead of the original 28 sets of capacitance values to measure the oil–gas two-phase flow parameters.

This article proposes an EARM algorithm. The Grad-CAM model is used to visually analyze the CNN network flow pattern identification, and the main focus of CNN network flow pattern identification is searched by the flow pattern heatmap. Combined with the principle of ECT sensor image reconstruction, according to the hotspot distribution of the flow pattern heatmap, we find the flow pattern area that contributes the most to the flow pattern identification of the CNN network, and find the electrode pair distribution corresponding to the flow pattern area. Finally, the EARM algorithm is proposed, and the distribution of electrode pairs in the key identification area is reversed according to the flow pattern of the key identification area, which improves the characteristic quality of the ECT sensor oil–gas two-phase flow parameter measurement, making the characteristics used for parameter measurement more prominent. Therefore, the accuracy of the measurement of oil–gas two-phase flow parameters is improved. Section 5 introduces the experimental results of oil–gas two-phase flow measurement by the EARM algorithm, and designs a control group experiment to compare with the measurement results of the EARM algorithm, and finally explores the relevant factors that may affect the hotspot distribution of the flow pattern heatmap.

5. Results and analysis

5.1. EARM algorithm prediction results

Section 4 introduces the ECT sensor electrode pairs that need to be extracted when using the EARM algorithm to measure the oil–gas two-phase flow parameters under different gas flow rate conditions. In this experiment, the capacitance value obtained by the EARM algorithm and the original 28 capacitance values of the ECT sensor are compared and analyzed. Through the Lenet-5 model in the CNN network, the oil–gas two-phase flow parameters are measured according to the capacitance value obtained by the EARM algorithm and the original 28 capacitance values of the ECT sensor, and the measurement results under different gas flow rate conditions are analyzed.

5.1.1. Measurement results of the ECT sensor upstream of the venturi tube. Figure 13 respectively shows the measurement accuracy of the oil flow rate and gas flow rate of the oil–gas two-phase flow under the conditions of small, medium, and large gas flow rate in the ECT sensor upstream of the venturi tube.

According to the experimental results in table 1, the predicted relative errors under different gas flow rate conditions are measured. The abscissa in figure 13 represents different experimental working conditions, and the ordinate represents the average predicted relative error under different experimental working conditions. There are 8000 sets of training data and 2000 sets of test data under each experimental working condition, respectively. Each vertex on the curve in figure 13 represents the average prediction relative error under this experimental working condition, which can be credible.
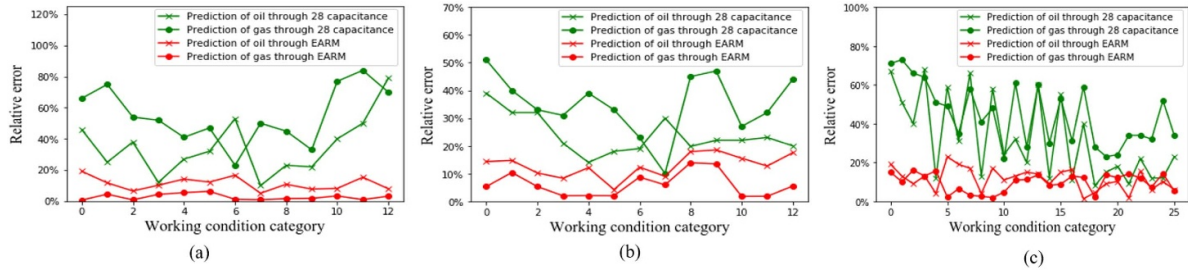
Figure 13. The relative error of the capacitance data prediction of the ECT sensor upstream of the venturi tube. (a) The prediction results of 28 original capacitance values and the EARM algorithm under small gas flow rate. (b) The prediction results of 28 original capacitance values and the EARM algorithm under medium gas flow rate. (c) The prediction results of 28 original capacitance values and the EARM algorithm under large gas flow rate.

The following figures 14–16 have the same physical meaning. As can be seen from figure 13, relative to the prediction effect of the original 28 capacitance values of the ECT sensor, the flow rate prediction relative error of the EARM algorithm is significantly reduced, and the relative error reduction effect of the gas flow rate prediction is more significant. Under the condition of small gas flow rate, the prediction improvement effect of the EARM algorithm is more significant, where the relative error of gas flow rate prediction is less than 5%, and the relative error of oil flow rate prediction is less than 15%. It can be seen that the EARM algorithm can obtain the key flow pattern area of the CNN network flow pattern identification. This method can effectively improve the feature quality of oil–gas two-phase flow prediction, and greatly improve the prediction accuracy of the oil flow rate and gas flow rate.

The following analyzes the improvement effect of the capacitance value extracted by the EARM algorithm relative to the original 28 capacitance measurement results of ECT under different gas flow rate conditions. By comparing the average parameter lifting index (APLI) of the EARM algorithm with respect to the original 28 capacitance value prediction effects, the parameter prediction improvement effect of the EARM algorithm under different gas flow rate conditions is compared. The calculation method of the APLI is shown in formula (5).

$$APLI = mean(|RE_{original} - RE_{EARM}|/RE_{original}) \quad (5)$$

Among them, APLI represents the average parameter lifting index of the EARM algorithm, $RE_{original}$ represents the relative error of the parameter prediction using the original 28 capacitances, and RE_{EARM} represents the relative error of the parameter prediction using the EARM algorithm.

Table 2 shows the APLI of the oil–gas two-phase flow parameters predicted by the EARM algorithm under different gas flow rate conditions.

It can be seen from table 2 that by comparing the APLI under different gas flow rate conditions, for the capacitance data of the ECT sensor upstream of the venturi tube, under the condition of small gas flow rate, the APLI of the oil flow rate and gas flow rate is the highest, indicating that the parameter prediction effect of the EARM algorithm is the best under the condition of small gas flow rate. For all gas flow rate conditions, the APLI of gas flow rate prediction is higher than that

of oil flow rate prediction, indicating that the EARM algorithm has a more obvious effect on gas flow rate prediction.

5.1.2. Measurement results of the ECT sensor downstream of the venturi tube. Compared with the flow pattern heatmap analysis results of the ECT sensor upstream of the venturi tube, the hotspot distribution of the flow pattern heatmap downstream of the venturi tube is more concentrated. Figure 14 respectively shows the measurement accuracy of the oil flow rate and gas flow rate of the oil–gas two-phase flow under the conditions of small gas flow rate and large gas flow rate in the ECT sensor downstream of the venturi tube.

Figure 14 shows the relative error of the capacitance data prediction of the ECT sensor downstream of the venturi tube under different gas flow rate conditions. As can be seen from figure 14, for the capacitance data of the ECT sensor downstream of the venturi tube, the prediction relative error of the EARM algorithm relative to the original 28 capacitance values is significantly improved; among them, the improvement effect of gas flow rate prediction is more obvious. This phenomenon proves the universality of the EARM algorithm. The prediction accuracy of oil–gas two-phase flow at small gas flow rate is better than that at large gas flow rate. Under the condition of small gas flow rate, more than 90% of the prediction accuracy of the gas flow rate is less than 5% and more than 90% of the prediction accuracy of the oil flow rate is less than 15%. For the capacitance values of the ECT sensors upstream and downstream of the venturi tube, the prediction accuracy of the oil flow rate and gas flow rate of the oil–gas two-phase flow by the EARM algorithm has been significantly improved.

The following is an analysis of the APLI of the prediction effect of the EARM algorithm relative to the original 28 capacitance values. Table 3 shows the APLI of the ECT sensor capacitance data downstream of the venturi tube under the conditions of different gas flow rate to predict the parameters of the oil–gas two-phase flow.

It can be seen from table 3 that for the capacitance data of the ECT sensor downstream of the venturi tube, under the condition of small gas flow rate, the APLI of gas flow rate prediction is higher. Under the condition of large gas flow rate, the APLI of oil flow rate prediction is higher. It shows that under the condition of small gas flow rate, the effect of the EARM algorithm on gas flow rate prediction is more

Table 2. EARM algorithm analysis table of APLI of upstream ECT sensor.

Parameter Different situation	Small gas flow rate	Medium gas flow rate	Large gas flow rate
$APLI_{oil}$	0.6104	0.4260	0.5472
$APLI_{gas}$	0.9469	0.8071	0.7625

(a)   (b)
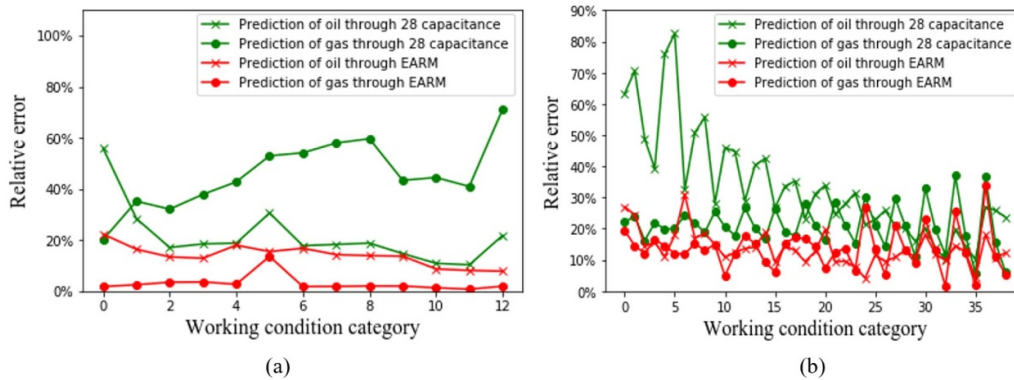
Figure 14. The relative error of the capacitance data prediction of the ECT sensor downstream of the venturi tube. (a) The prediction results of 28 original capacitance values and the EARM algorithm under small gas flow rate. (b) The prediction results of 28 original capacitance values and the EARM algorithm under large gas flow rate.

Table 3. EARM algorithm analysis table of APLI of downstream ECT sensor.

Parameter Different situation	Small gas flow rate	Large gas flow rate
$APLI_{oil}$	0.2877	0.5241
$APLI_{gas}$	0.9305	0.3672

obvious, and under the condition of large gas flow rate, the effect of EARM algorithm on oil flow rate prediction is more obvious.

The EARM algorithm is used to analyze the capacitance data of the ECT sensors upstream and downstream of the venturi tube. Compared with the original 28 capacitance values for parameter prediction, the EARM algorithm has a better improvement effect on the measurement of oil–gas two-phase flow parameters. This shows that the CNN network visualization method combined with the ECT image reconstruction principle for comprehensive analysis is effective. Deeply mining the relationship between the CNN network and the ECT image reconstruction physical principles has a significant improvement effect on the parameter measurement of oil–gas two-phase flow. This phenomenon can also be used in the research of more multiphase flow fields such as ECT image reconstruction, parameter measurement, flow pattern identification and so on.

5.2. Experimental prediction results of the control group

In order to verify the measurement performance of the EARM algorithm, this paper compares the experimental results through the control group experiment. The EARM algorithm uses the CNN and Grad-CAM model to extract the hotspots

of the flow pattern heatmap, so as to find the most effective flow pattern area that affects the flow pattern identification, and reverse mapping to obtain the capacitance value corresponding to the flow pattern area. In the control group experiment, this paper uses the capacitance data that doe not completely cover the flow pattern hotspot area (control group 1) and the capacitance data that exceed the flow pattern hotspot area (control group 2) as the control groups, explores the prediction results of these two sets of capacitance data, and compares the measurement performance of the EARM algorithm.

Based on the prediction results of section 5.1, it can be seen that the flow patterns upstream and downstream of the venturi tube have better prediction results under the EARM algorithm, and the prediction trends are the same. Therefore, in the control group experiment, we only analyzed the flow pattern data upstream of the venturi tube. Figure 15 shows the prediction results of control group 1 under different gas flow rate conditions.

Control group 1 is an experimental group using capacitance data that doe not completely cover the hotspot area of the flow pattern. It can be seen from the comparison results of the relative error between control group 1 and the EARM algorithm test group that the prediction results of the oil–gas two-phase flow parameters are inferior to the prediction results of the flow pattern hotspot area. However, the prediction results of the oil–gas two-phase flow parameters of control group
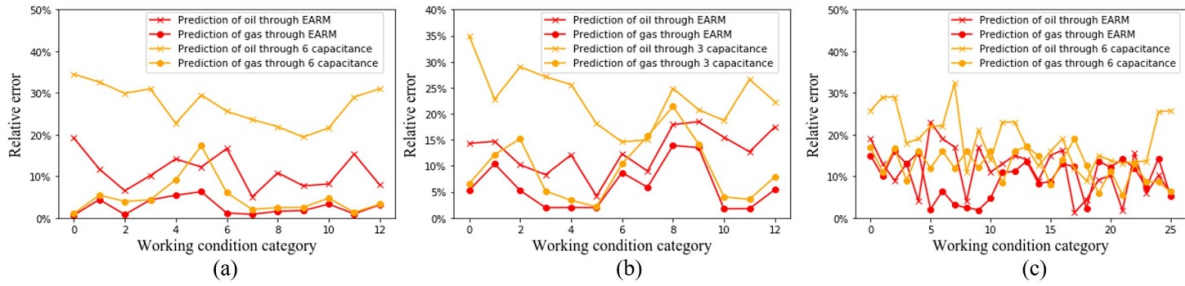
Figure 15. Relative error of control group 1 experiments. (a) Predicted results of comparative experiments under small gas flow rate. (b) Predicted results of comparative experiments under medium gas flow rate. (c) Predicted results of comparative experiments under large gas flow rate.
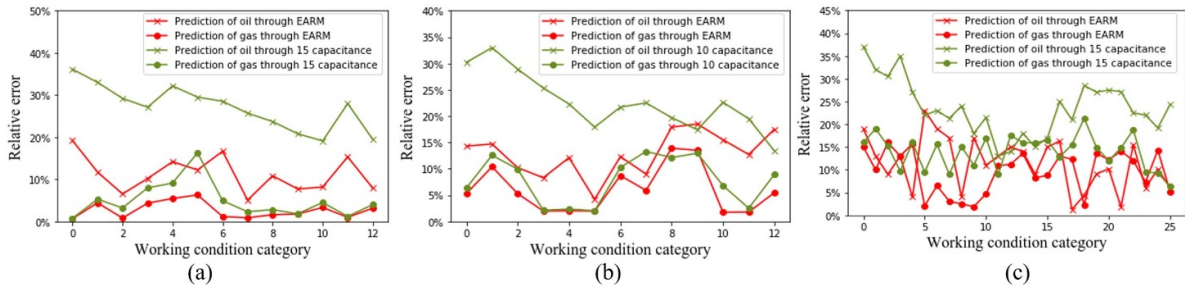
Figure 16. Relative error of control group 2 experiments. (a) Predicted results of comparative experiments under small gas flow rate. (b) Predicted results of comparative experiments under medium gas flow rate. (c) Predicted results of comparative experiments under large gas flow rate.

1 are better than those using the original 28 capacitance values, which shows that the extraction of more critical information of the flow pattern to a certain extent is effective for the prediction of oil–gas two-phase flow parameters. In addition, the effectiveness of the extracted key information determines the improvement degree of the oil–gas two-phase flow parameter prediction effect. The experimental results of control group 2 are analyzed below. Figure 16 shows the prediction results of control group 2 under different gas flow rate conditions.

Control group 2 is an experimental group using capacitance data exceeding the flow pattern hotspot area. It can be seen from the comparison results of the relative errors between control group 2 and the EARM algorithm test group that for the capacitance data that exceeds the flow pattern hotspot area, the prediction results of the oil–gas two-phase flow parameters are inferior to the prediction results of the flow pattern hotspot area. As with control group 1, the prediction result of control group 2 is also better than the flow prediction results using the original 28 capacitance values. The experimental results of the two control groups can prove that the capacitance value of the effective area of the flow pattern extracted by the EARM algorithm is reasonable. The hotspot area of the flow pattern extracted beyond this area or less than this area will affect the oil–gas two-phase flow parameter prediction results. However, the extraction of effective flow pattern information through the CNN network visualization algorithm will improve the prediction effect of oil–gas two-phase flow parameters. The following will analyze and explore the factors that may affect the hotspot distribution of the flow pattern heatmap.

5.3. Research on related factors of hotspot distribution

Under different gas flow rate conditions, the distribution of hotspots in the ECT sensor flow pattern heatmap is different. According to the distribution of hotspots in the heatmap, combined with the principle of ECT image reconstruction, this paper explores the factors that may affect the distribution of hotspots in flow patterns. It can be seen from figures 4 and 5 that in the case of small gas flow rate, the hotspot distribution of the flow pattern heatmap is not stable. As the gas flow rate increases, the hotspots of the flow pattern heatmap are stable, and the hotspots of the flow pattern are distributed on the upper side or the upper left side of the flow pattern. According to this phenomenon, we can infer that the focus of the CNN network for flow pattern identification is concentrated in the area of gas distribution in the flow pattern. The flow rate and distribution of gas in the oil–gas two-phase flow play a vital role in the CNN network to determine the flow pattern. When judging the annular flow, there is always oil in the lower area of the flow pattern. Therefore, judging whether there is oil on the upper side of the flow pattern and whether the oil in the flow pattern forms a ring is an important basis for CNN network flow pattern identification. For stratified flow and slug flow, the hotspots of the flow pattern heatmap are mainly located at the boundary between the oil phase and the gas phase, indicating that the gas flow rate and position distribution are also the main concerns of the CNN network flow pattern identification. The above analysis is just a qualitative analysis of the influencing factors of hotspot distribution of flow pattern heatmaps based

on experimental phenomena. In future experimental work, we will conduct a quantitative analysis of the specific causes of the hotspot distribution of the flow pattern heatmap, and prove the reasons for the different hotspot distributions of the flow pattern heatmap under different flow rates.

6. Conclusion

In this paper, we combine the CNN network visualization with the physical principles of ECT image reconstruction, and propose an EARM algorithm for extracting key flow pattern information for oil- gas two-phase flow pattern identification. The flow pattern heatmap is obtained by the Grad-CAM method. By analyzing the hotspot information distribution of the flow pattern heatmap, the main flow pattern identification area of CNN network flow pattern identification is found, and the effective capacitance value corresponding to the flow pattern position is extracted according to the image reconstruction principle. By using the EARM algorithm, the predicted results of the effective capacitance value extracted are compared with the predicted results of the ECT sensor original capacitance value. The EARM algorithm effectively extracts the effective capacitance information of the flow pattern identification, and the measurement result of the oil–gas two-phase flow parameters have been significantly improved by more than 50% on average. We also designed two sets of control group experiments in this study, which proved that the range of the extracted key flow pattern area is reasonable. This paper qualitatively analyzes the reasons that may affect the hotspot distribution of the flow pattern heatmap.

In future research, we will further quantitatively analyze the reasons for the hotspot distribution of the flow pattern heatmap, and explore the specific reasons for the different hotspot distributions of the flow pattern heatmap at different flow rates.

Acknowledgments

ORCID iD

Yi Li ⓘ https://orcid.org/0000-0002-8855-4520

References

[1] Oddie G and Pearson J A 2004 Flow-rate measurement in two-phase flow *Annu. Rev. Fluid Mech.* **36** 149–72

[2] Zhang L and Wang H 2010 Identification of oil–gas two-phase flow pattern based on svm and electrical capacitance tomography technique *Flow Meas. Instrum.* **21** 20–4

[3] Vuong D H, Sarica C, Pereyra E and Al-Sarkhi A 2018 Liquid droplet entrainment in two-phase oil-gas low-liquid-loading flow in horizontal pipes at high pressure *Int. J. Multiph. Flow* **99** 383–96

[4] Sharaf S, Da Silva M, Hampel U, Zippe C, Beyer M and Azzopardi B 2011 Comparison between wire mesh sensor and gamma densitometry void measurements in two-phase flows *Meas. Sci. Technol.* **22** 104019

[5] Zhao C, Wu G and Li Y 2019 Measurement of water content of oil-water two-phase flows using dual-frequency microwave method in combination with deep neural network *Measurement* **131** 92–9

[6] Dong X, Tan C, Yuan Y and Dong F 2015 Measuring oil–water two-phase flow velocity with continuous-wave ultrasound doppler sensor and drift-flux model *IEEE Trans. Instrum. Meas.* **65** 1098–107

[7] Da Silva M, Thiele S, Abdulkareem L, Azzopardi B and Hampel U 2010 High-resolution gas–oil two-phase flow visualization with a capacitance wire-mesh sensor *Flow Meas. Instrum.* **21** 191–7

[8] López J, Pineda H, Bello D and Ratkovich N 2016 Study of liquid–gas two-phase flow in horizontal pipes using high speed filming and computational fluid dynamics *Exp. Therm. Fluid Sci.* **76** 126–34

[9] Rahiman M H F, Rahim R A, Rahiman M H F and Tajjudin M 2006 Ultrasonic transmission-mode tomography imaging for liquid/gas two-phase flow *IEEE Sens. J.* **6** 1706–15

[10] Meng Z, Huang Z, Wang B, Ji H, Li H and Yan Y 2010 Air–water two-phase flow measurement using a venturi meter and an electrical resistance tomography sensor *Flow Meas. Instrum.* **21** 268–76

[11] Li X, Huang Z, Wang B and Li H 2008 A new method for the online voidage measurement of the gas–oil two-phase flow *IEEE Trans. Instrum. Meas.* **58** 1571–7

[12] Arirachakaran S, Oglesby K, Malinowsky M, Shoham O and Brill J *et al* 1989 An analysis of oil/water flow phenomena in horizontal pipes *SPE Production Symp.* pp 1–13

[13] Angeli P and Hewitt G 1999 Pressure gradient in horizontal liquid–liquid flows *Int. J. Multiph. Flow* **24** 1183–203

[14] Delnoij E, Kuipers J, van Swaaij W P M and Westerweel J 2000 Measurement of gas–liquid two-phase flow in bubble columns using ensemble correlation PIV *Chem. Eng. Sci.* **55** 3385–95

[15] Lovick J and Angeli P 2004 Droplet size and velocity profiles in liquid–liquid horizontal flows *Chem. Eng. Sci.* **59** 3105–15

[16] Charles M T and Lilleleht L 1966 Correlation of pressure gradients for the stratified laminar-turbulent pipeline flow of two immiscible liquids *Can. J. Chem. Eng.* **44** 47–9

[17] Augier F, Guiraud P and Masbernat O 2007 Velocity fluctuations in a homogeneous dispersed liquid–liquid flow at high phase fraction *Phys. Fluids* **19** 057105

[18] Hanafizadeh P, Eshraghi J, Taklifi A and Ghanbarzadeh S 2016 Experimental identification of flow regimes in gas–liquid two phase flow in a vertical pipe *Meccanica* **51** 1771–82

[19] Roshani G, Nazemi E, Feghhi S and Setayeshi S 2015 Flow regime identification and void fraction prediction in two-phase flows based on gamma ray attenuation *Measurement* **62** 25–32

[20] Hu H, Dong J, Zhang J, Cheng Y and Xu T 2011 Identification of gas/solid two-phase flow regimes using electrostatic sensors and neural-network techniques *Flow Meas. Instrum.* **22** 482–7

[21] Zhou Y and Gu Y 2012 Flow regime identification of gas/liquid two-phase flow based ICA and RBF neural networks *CIESC J.* **63** 796–9

[22] Krizhevsky A, Sutskever I and Hinton G E 2012 Imagenet classification with deep convolutional neural networks *Adv. Neural Inf. Process. Syst.* **2** 1097–105

[23] Gu Z, Eils R and Schlesner M 2016 Complex heatmaps reveal patterns and correlations in multidimensional genomic data *Bioinformatics* **32** 2847–9

[24] Selvaraju R R, Cogswell M, Das A, Vedantam R, Parikh D and Batra D 2017 Grad-cam: visual explanations from deep

networks via gradient-based localization *Proc. of the IEEE International Conference on Computer Vision* pp 618–26

[25] Yang X, Zhao C, Chen B, Zhang M and Li Y 2019 Big data driven u-net based electrical capacitance image reconstruction algorithm *2019 IEEE Int. Conf. on Imaging Systems and Techniques (IST)* IEEE pp 1–6

[26] Xu Z, Yang X, Chen B, Zhang M and Li Y 2019 Imaging of flow pattern of gas-oil flows with convolutional neural network *2019 IEEE Int. Conf. on Imaging Systems and Techniques (IST)* IEEE pp 1–6

[27] Tan C, Lv S, Dong F and Takei M 2018 Image reconstruction based on convolutional neural network for electrical resistance tomography *IEEE Sens. J.* **19** 196–204

[28] Dang W, Gao Z, Hou L, Lv D, Qiu S and Chen G 2019 A novel deep learning framework for industrial multiphase flow characterization *IEEE Transactions on Industrial Informatics* **15** 5954–62

[29] Du M *et al* 2018 Oil-in-water two-phase flow pattern identification from experimental snapshots using convolutional neural network *IEEE Access* **7** 6219–25

[30] Yang Y and Peng L 2013 Data pattern with ECT sensor and its impact on image reconstruction *IEEE Sens. J.* **13** 1582–93

[31] Xu Z, Wu F, Yang X and Li Y 2020 Measurement of gas-oil two-phase flow patterns by using CNN algorithm based on dual ECT sensors with venturi tube *Sensors* **20** 1200